Loss of cell polarity regulators initiates pyroptosis in trophoblasts at the human maternal fetal interface

Authors: Khushali Patel[2,4], Jasmine Nguyen[1,4], Sumaiyah Shaha[1], Ashley Zubkowski,[3] Meghan Riddell[1,2]

Affiliations:
1) Department of Physiology, University of Alberta, Canada, T6G 2S2
2) Department of Obstetrics and Gynecology, University of Alberta, Canada, T6G 2S2
3) Department of Biological Sciences, University of Alberta, Canada, T6G 2S2
4) These authors contributed equally to this work

Corresponding Author:
Meghan Riddell
Address: 227 Heritage Medical Research Centre, University of Alberta, T6G 2S2
Phone: (780)-492-8561
Email: mriddell@ualberta.ca

Abstract:

The syncytiotrophoblast is a single giant multinucleate epithelial cell that forms the maternal surface of the human placenta and is bathed in maternal blood. It acts as a physical barrier between the maternal and fetal compartments and facilitates nutrient and waste exchange. As such, syncytiotrophoblast dysfunction is a key feature of pregnancy pathologies, such as preeclampsia. An understudied feature of dysfunctional syncytiotrophoblast is the loss of apical microvilli. But a paucity of data exists about the mechanisms regulating syncytiotrophoblast microvilli maintenance. Atypical protein kinase-c (aPKC) isoforms are evolutionarily conserved apical polarity regulators, which are known to play a role in the regulation of intestinal microvilli. Thus, we hypothesized that aPKC isoforms regulate syncytiotrophoblast microvilli and apical surface structure. Using human placental explant culture and primary human trophoblasts, we found that aPKCs regulate the structure, permeability, and endocytic function of the syncytiotrophoblast apical surface in a spatially restricted manner.

A heightened inflammatory environment is often involved in the pathogenesis of placental pathologies, and the pro-inflammatory cytokine TNF-α can decrease aPKC-ι expression in intestinal cells. Here we establish that TNF-α exposure leads to reduced expression of the aPKC-ι isoform in syncytiotrophoblast and profoundly alters ST apical structure and permeability via regionalized pyroptosis, a highly pro-inflammatory form of cell death. Therefore, this is the first work to identify a regulator of apical-surface structure and the induction of the pyroptotic cascade at the maternal surface of the human placenta.

Keywords: Placenta, aPKC, trophoblast, microvilli, pyroptosis, TNF-α, Gasdermin-E

Introduction:

The placenta is a fetally-derived transient organ that performs critical functions like gas and nutrient exchange, pregnancy supporting hormone secretion, and acts as a physical barrier between the maternal and fetal compartments to establish and maintain a healthy pregnancy(1). The maternal-facing surface of the human placenta is covered by a single giant multinucleated epithelial cell called the syncytiotrophoblast (ST), which measures up to $10m^2$ by the end of gestation(2). The ST is a highly polarized epithelial cell with dense apical microvilli decorating its surface, but it lacks lateral membranous barriers between nuclei. Thus, the ST represents a completely unique type of epithelial barrier. Since the ST cannot undergo mitosis, it is maintained by the fusion of underlying proliferative-mononuclear progenitor cytotrophoblasts. The ST is the primary cell-type responsible for carrying out the essential placental functions listed above, therefore ST stress and dysfunction is a key feature of common pregnancy complications like preeclampsia and intrauterine growth restriction(3-6).

Polarity is a particularly important characteristic of epithelial cells, such as the ST. Cell polarity is the spatial asymmetric organization of biomolecules and cellular components in the cell. Apical-basal polarity is the formation and maintenance of discrete structure and function of the apical and basal surface of a cell and is a hallmark feature of many epithelia. In particular, the apical surface is dominated by microvilli, which are membrane protrusions supported by a core bundle of actin filaments (F-actin)(7, 8). Critically, active maintenance of cell polarity is important to support microvillar structural integrity. For example, microvillar F-actin cross-linkage to the cell membrane by linker

proteins from the ezrin, radixin and moesin (ERM) family must be maintained via phosphorylation(7, 9, 10). Microvilli functionally increase the surface area of a cell to facilitate gas and nutrient exchange, are a site of endocytosis and signal transduction, and may be the site of extracellular vesicle release in the ST(11, 12). As such, disturbances in microvillar maintenance can lead to impaired cellular functions such as disturbed fluid and nutrient uptake as well as impaired transport and secretion(13-15). Importantly, disruption of ST microvillar structure has been reported in placentas from intrauterine growth restriction and preeclampsia pregnancies(3, 16-19). However no studies have directly examined the mechanisms regulating maintenance of ST polarity and microvilli.

In epithelial cells, apical-basal polarity establishment and maintenance is governed by evolutionarily conserved protein complexes. One such functional module is the Par complex that includes the scaffolding proteins partitioning defective-3 (Par-3), partitioning defective -6 (Par-6), and a Ser/Thr kinase, atypical protein kinase C (aPKC). The Par complex localizes apically and alongside the Crumbs complex establishes and maintains apical identity in multiple epithelial cell types (20-22). The Par complex serves to localize and activate the aPKC isoforms. Critically, aPKCs have been shown to regulate apical polarity by inhibiting localization of basal domain determining proteins such as Lgl, Numb, and Miranda in various epithelial cells(22), including the trophectoderm, which is the precursor cell-type to trophoblasts(23). APKC-ι and aPKC-ζ are the two major aPKC isoforms found in humans. We have previously shown that three isoforms of aPKC are expressed in ST: aPKC-ι, aPKC-ζ, and a novel N-terminal

truncated *PRKCZ* encoded isoform – aPKC-ζ III(24). aPKC-ζ III lacks the N-terminal PB-1 domain required for Par-6 binding(24, 25). Hence, it is presently unclear if it can be fully activated since interaction with binding partners via this domain is thought to be required for the removal of the pseudosubstrate inhibitory domain and the full activation of aPKC isoforms(25, 26). Importantly, aPKC isoforms have both individual and redundant functions. As such, the aPKC-ζ global knockout mice have no embryonic phenotype(27, 28), whereas aPKC-λ/ι global knockout mice are embryonic lethal at ~E9 with severe growth restriction and placental maternal-fetal interface malformation(29, 30). But, aPKC-ζ can partially compensate for aPKC- λ/ι knockout in mouse embryos(27), therefore consideration for isoform specific and total aPKC function is necessary. Bhattacharya *et.al* found that placental specific knockout of aPKC-λ/ι as well as global aPKC-λ/ι knockout lead to a lack of labyrinthine zone development, the primary zone for maternal/fetal exchange in mice(29). They also found that knockdown of *PRKCI* in human trophoblast stem cells decreased their ability to fuse and form ST, revealing an important role for aPKC-ι in maternal-fetal interface formation(29). However, the function of all aPKC isoforms in the ST has not been addressed to date.

APKCs can play an important role in the activation of apical ERM proteins(31). Specifically, aPKC-ι/λ regulates the emergence and maintenance of intestinal microvilli by phosphorylating ezrin(31). As mentioned above, ezrin is a cytoskeletal linker protein that links the microvillar F-actin core to the cell membrane when activated via phosphorylation at Thr567 site(7, 9, 10). It is abundantly expressed at the ST apical surface at the end of gestation(32). APKCs are also involved in F-actin reorganization in

other tissues via other proteins such as Rac-1 and Rho family GTP-ases(21, 33-37), therefore it is highly plausible that aPKC isoforms regulate ST apical identity via similar pathways.

Alterations in aPKC expression and/or mis-localization of aPKCs from the apical membrane are associated with multiple human pathologies such as cancer, irritable bowel syndrome and microvillar inclusion disease(38-41). Critically, a pro-inflammatory cytokine – tumor necrosis factor-α (TNF-α) has been shown to decrease aPKC-ι apical expression in intestinal cells via post-translational proteasomal dependent mechanisms(42). Elevated maternal circulating levels of TNF-α are associated with placental pathologies such as preeclampsia(43) and treatment of pregnant baboons and rats with TNF-α early in gestation can induce preeclampsia-like phenotypes (44, 45). TNF-α has also been shown to play a key role in inflammation-induced animal models of fetal loss, growth restriction, and preeclampsia-like phenotypes(46, 47). Thus, disruption of aPKC isoforms could play an un-recognized role in the development of placental disorders.

In this study we sought to identify whether aPKC isoforms regulate apical polarization and microvillar organization of the ST. Our study reveals that aPKC isoform activity and expression is critical for the maintenance of the ST apical surface structure, integrity, and function in a regionalized manner. Moreover, we show that TNF-α regulates ST aPKC-ι expression, and that TNF-α and loss of aPKC activity led to regionalized loss of

ST microvilli and apical membrane integrity due to the induction of non-classical pyroptosis.

Results:

Our initial studies examining aPKC isoforms in the human placenta revealed an apparent lack of anti-aPKC-ι or anti-aPKC-ζ/ζ III signal accumulation at the ST apical membrane in early first trimester placental samples(24). In other cell types, apical localization is required for aPKC's to regulate apical-basal polarity, as mentioned above. Thus, we first performed colocalization analyses using antibodies targeting aPKC-ι or aPKC-ζ isoforms (which we previously validated to recognize aPKC-ζ and aPKC- ζ III (24)) and an anti-ezrin antibody, an established ST apical membrane marker in third trimester placenta(32). As we observed previously(24), the anti-aPKC-ι signal was weak and largely diffuse within the ST from 4-6 weeks gestation (Supplementary Figure 1A). There was also a lack of consistent apical accumulation of anti-ezrin signal at the ST apical surface despite a highly accumulated and complex pattern of anti-β-actin signal in the apical region (Supplementary Figure 1A). By 7-8 weeks gestation, both anti-aPKC-ι and anti-ezrin signal had strong regional apical accumulation with a significantly increased colocalization compared to 4-6 weeks gestation (Figure 1B, Supplementary Figure S1A), though areas where an apical anti-ezrin signal was absent were consistently observed at all gestational ages examined. Similar apical localization and aPKC-ι:ezrin colocalization coefficients were quantified in 9-12 week and 37-40 week ST, though the signal was more consistently apical between biological replicates (Figure 1 A,B). Apical accumulation of anti-aPKC-ζ signal followed a similar trend, with a

significant increase in the apical aPKC-ζ:ezrin colocalization coefficient by 7-8 weeks gestation (Figure 1D, Supplementary Figure S1B) that did not vary significantly at 9-12 weeks or 37-40 weeks gestation (Figure 1C-D).

Having established that aPKC isoforms and ezrin strongly and consistently colocalize at the ST apical surface from 9 weeks gestation, we used floating placental explant culture and a myristoylated aPKC pseudosubstrate inhibitor (aPKC inhibitor), which blocks both aPKC-ι and aPKC-ζ activity(48), to test if aPKC's may regulate ST apical membrane structure via ezrin phosphorylation, as observed during murine intestinal development (31). After 6 hours of treatment, a significant decrease in the ST anti-phospho Thr-567 ezrin to total ezrin signal as well as the total anti-ezrin signal was observed in both 9-12 week and 37-40 week aPKC inhibitor vs. control treated explants (Figure 2A-E, Supplementary Figure S2). AKT was previously shown to regulate ezrin phosphorylation at Thr567 in a trophoblastic cell line(49), so we also confirmed that aPKC inhibitor treatment did not alter the activity of AKT in 9-12 week placental explants (Supplementary Figure S3A,B). Thus, aPKC kinase activity regulates the expression of ezrin as well as it's phosphorylation at Thr-567 in ST. In addition to the effects on ezrin, we also noted an appreciable decrease and change in signal pattern for apical ST anti-β-actin signal with aPKC inhibitor treatment (Figure 2A). Therefore we quantified the amount of ST apical F-actin in aPKC inhibitor treated explants using phalloidin. APKC inhibitor led to a more than 50% decrease of ST apical phalloidin signal intensity in both first trimester and term explants (Figure 2F-H, Supplementary Figure S4A). Areas without appreciable apical-phalloidin signal were interspersed with regions with clearly

decreased, or undetectable, phalloidin signal. Significantly reduced apical phalloidin intensity was also observed after both 2 and 4 hours aPKC inhibitor treatment without the appearance of seemingly phalloidin-devoid regions (Supplementary Figure S4B-D).

To address aPKC isoform-specific roles in ST, we performed siRNA mediated knockdown. 9-12 weeks explants were treated with siRNA targeting *PRKCI* and/or *PRKCZ*. Knockdown efficiency for aPKC-ι, aPKC-ζ, and aPKC-ζ III was determined by western blot analyses of explant lysate (Figure 2I-P), where a significant decrease in all isoforms was consistently achieved. Importantly, this method targets siRNA to the ST and leads to limited, but variable, accumulation of siRNA in the underlying cytotrophoblast progenitor cells that also express all three aPKC isoforms(24, 50), hence the moderate knockdown efficiency obtained. Treatment with *PRKCI* siRNA, *PRKCZ* siRNA, or both lead to significantly decreased ST apical phalloidin mean intensity (Figure 2Q-R). Importantly, as with aPKC inhibitor treatment, the appearance of seemingly-phalloidin replete areas was also regionally specific with siRNA knockdown. Additionally, no change in the apparent thickness of the ST could be observed using wheat germ agglutinin (WGA-lectin; Figure 2Q), a lectin that binds to the apical surface and cytoplasm of the ST (51, 52). Areas of ST denudation were not observed in scrambled control or siRNA-treated floating explants. These data suggest that even with the longer-culture timeline required to achieve peak siRNA knockdown, the ST was intact but has significantly depleted apical F-actin. A significant decrease in apical F-actin was observed with individual application of *PRKCI* siRNA and *PRKCZ* siRNA and no additive effect was observed with the addition of both. This suggests that

reduced expression of a single isoform is sufficient to alter the ST apical actin cytoskeletal dynamics and that aPKC isoforms redundantly regulate ST apical membrane F-actin abundance.

To confirm if loss of aPKC kinase activity leads to alterations in the ST apical membrane structure we performed electron microscopy on control and aPKC inhibitor treated first trimester placental explants. Scanning electron micrographs (SEM) revealed a severe loss of microvilli at the ST apical surface with inhibitor treatment, apparent coalition of the few remaining microvilli and a porous appearance of the apical membrane (Figure 3A, Supplementary Figure S5) in a region-specific manner. Transmission electron microscopy micrographs (TEM) confirmed the simplification of the apical surface structure apparent by SEM and revealed a ST specific loss of cytoplasmic density, a high abundance of variably-sized membrane coated vesicles, and swollen mitochondria (Figure 3B). Underlying cytotrophoblast progenitor cells did not have appreciable changes in any of these parameters and the basement membrane thickness between the cells did not vary between treatment groups.

Since SEM and TEM imaging revealed a regionalized decrease in cytoplasmic density and an almost lace-like appearance in the apical membrane we hypothesized that there is an increased permeability in ST with inhibition of aPKC's. Indeed, aPKC inhibitor treatment and *PRKCI*+*PRKCZ* siRNA knockdown both lead to a 4-fold increase in the uptake of 10,000MW neutral dextran (Figure 3C-F) compared to controls. *PRKCI* and *PRKCZ* siRNA treated samples also displayed a significant *2*.7 and 2.4-fold increase in

sum dextran signal (Figure 3E,F). Moreover, control explants displayed a punctate dextran signal localized to the apical surface of the ST, consistent with macropinocytotic uptake(53), whereas dextran signal for aPKC inhibitor and *PRKCI, PRKCZ, and PRKCI+PRKCZ* siRNA treated explants had a relatively diffuse signal. Importantly, this diffuse pattern of dextran uptake was restricted to areas of the ST lacking a visible continuous apical phalloidin signal. Thus, decreased aPKC isoform kinase activity or expression disrupts ST apical membrane integrity and permeabilizes the ST to a neutrally charged 10,000 dalton compound.

In addition to the effects on the apical membrane, TEM also revealed the appearance of highly variably sized cytoplasmic membrane coated vesicles (Figure 3B). In combination with the data showing altered F-actin abundance we hypothesized that loss of aPKC activity may lead to disrupted ST endocytic trafficking. Interestingly, we saw an increase in the colocalization of fluorescently-conjugated transferrin with anti-early-endosome antigen-1 (EEA1) when a transferrin uptake assay was performed on first trimester explants, suggesting an increase in clathrin-mediated transferrin endocytosis with aPKC inhibitor treatment (Figure 3G,H; Supplementary Figure S6A-E). There were also enlarged areas of anti-EEA1 signal at the ST apical surface in first trimester explants treated with aPKC inhibitor (Figure 3G; Supplementary Figure S6B,D). Interestingly, these enlarged EEA1 signals were not exclusively associated with regions of the ST with visibly decreased phalloidin signal. These data suggest that inhibition of aPKC's dysregulates ST clathrin-mediated endocytosis and leads to an increased endocytic activity or stalling of endosomal trafficking in the apical compartment.

We reasoned that the altered vesicular trafficking and increased cellular permeability induced by aPKC inhibitor treatment may also lead to increased release of ST-derived factors. The ST produces several pregnancy-sustaining hormones, including the hormone human chorionic gonadotropin (hCG). Therefore, we quantified the release of the hCG-β subunit via ELISA in explant conditioned medium from control and aPKC inhibitor treated samples. As expected, aPKC inhibitor led to a nearly 3-fold increase of hCG-β in explant conditioned medium within 6 hours of treatment (Figure 3I). In summary, aPKC isoforms regulate the integrity of the apical membrane, vesicular trafficking within and structure of the apical compartment, likely via the regulation of F-actin and ezrin abundance.

TNF-α has been shown to decrease expression of aPKC-ι in Caco-2 cells(42), and is known to be elevated in the maternal circulation in established placental pathologies(43, 54) where regionalized loss of microvilli, reduced cytoplasmic density, and hyper-vesicular cytoplasm have also been observed in the ST(3, 17, 19). Hence, we hypothesized that TNF-α would also decrease the expression of aPKC isoforms in the ST. Interestingly, we found that treatment of *in vitro* differentiated primary ST with TNF-α led to a dose dependent significant decrease in aPKC-ι expression only (Figure 4A-D). Additionally, both 100pg/mL and 10ng/mL doses of TNF-α resulted in a regionalized but overall significant decrease in apical phalloidin in both first trimester and term explants within 6 hours of treatment (Figure 4E-G, Supplementary Figure S7A), like aPKC-inhibitor treatment or aPKC isoform siRNA knockdown (Figure 2). As expected,

SEM revealed a regionalized severe loss of microvilli at the ST apical surface with TNF-α treatment and a similar porous or lace-like appearance of the apical membrane (Figure 4H; Supplementary Figure S7A) like with aPKC-inhibitor treatment. To confirm if this led to ST permeabilization, we performed dextran uptake assays that revealed a diffuse and significantly increased dextran signal throughout the ST compared to control in both first trimester and term TNF-α-treated explants (Figure 4I-K, Supplementary Figure S7B). Thus, TNF-α leads to isoform specific dose dependent decrease in ST aPKC-ι expression as well as permeabilization and simplification of the ST apical surface.

Loss of aPKC expression/activity or exposure to TNF-α induce multiple forms of cell death, including apoptosis and pyroptosis, in other cell types(55-61). Pyroptosis is a pro-inflammatory form of cell death characterized by the appearance of membrane pores due to the cleavage and oligomerization of gasdermin family proteins(59, 62). Gasdermin pore formation leads to the permeabilization of the membrane to low molecular weight compounds(63), and the release of mature IL-1β and other damage associated molecular patterns (DAMPS)(62, 64, 65). Since TNF-α and aPKC inhibitor treatment both induced regionalized formation of pore-like structures and increased permeability we hypothesized that they were inducing ST pyroptosis. Interestingly, when IL-1β levels were tested in explant conditioned medium a significant increase was only observed in first trimester explant-conditioned medium, but not term explant conditioned medium for both aPKC inhibitor and TNF-α (Figure 5A-D). The ST has previously been shown to express gasdermin-D(66), therefore we stained TNF-α treated explants with

an anti-cleaved (Asp275) gasdermin-D (cl-GSDMD) antibody expecting to see an increase in cl-GSDMD signal at the ST apical membrane, since we had clearly demonstrated their increased permeability to dextran. In contrast to our hypothesis, no anti-cl-GSDMD signal could be observed within the ST, despite clear signal in both control and TNF-α treated cells in the villous core (Figure 5E). A similar staining pattern was observed in aPKC inhibitor treated explants (Supplementary Figure S8B). No cl-GSDMD signal was detected in tissue from that was fixed without culture whereas a stromal cl-GSDMD signal was observed in c explant cultured tissue from the same donor (Supplementary Figure S9). Gasdermin-E is a second gasdermin family member known to be expressed in the placenta(62). We first confirmed that it is expressed in the ST at both 9-12 weeks and 37-40 weeks gestation using an anti-gasdermin E antibody (Figure 5F-G; Supplementary Figure S10A-C), where a punctate signal pattern was observed. Importantly, enrichment of anti-gasdermin E signal was seen in discrete areas of the ST, as well as sporadic cytotrophoblast progenitor cells at all gestational ages examined (Supplementary Figure S10B). A clear anti-gasdermin E signal was also observed in cells within the placental core in term tissue (Supplementary Figure S10). Interestingly, TNF-α treatment led to an apparent aggregation of anti-GSDME signal into large high signal intensity puncti at the apical border of the accumulated dextran signal in first trimester explants (Figure 5F). A similar change in anti-gasdermin E signal was also observed in aPKC-inhibitor treated first trimester explants (Supplementary Figure S8C). These large apically-localized puncti were also occasionally observed in control treated explants. A similar change in localization of the anti-gasdermin E signal was not observed in term explants in either condition, with only rare large aggregates of anti-

gasdermin E signal observed in the apical region, though high-signal intensity aggregates were observed in the basal region of the ST (Figure 5G). To confirm if gasdermin-E cleavage occurs in the ST *in vitro* differentiated ST were treated with TNF-α and prepared for western blotting analysis. Both full-length gasdermin-E and p30 cleaved gasdermin-E bands were observed, with a 2 -fold increase in p30 gasdermin E in TNF-α treated cells (Figure 5H-I). Caspase-3 has been shown to cleave gasdermin E, allowing for oligomerization and pore formation(61, 67), therefore we used an anti-active caspase-3 antibody (cleaved caspase-3) to stain TNF-α and aPKC inhibitor treated explants. No signal could be detected within the ST in any treatment group in both first trimester and term explants (Figure 5J,K; Supplemental Figure S8E,F), though a clear signal could be detected in stromal cells, especially in TNF-α treated explants, consistent with previous studies showing caspase-3 activity is restricted to the cytotrophoblasts(68).

Dimethyl fumarate (DMF), an anti-inflammatory compound used to treat relapsing and remitting multiple sclerosis and psoriasis, has recently been identified as an anti-pyroptotic agent by blocking the cleavage of both gasdermin-D and -E via succination(69). As such, we sought to block TNF-α and aPKC inhibitor-induced pyroptosis by co-administration of the factors with DMF. As expected, DMF prevented TNF-α induced ST permeability to dextran in both first trimester and term explants (Figure 6 A,B; Supplemental Figure S11A,B). First trimester aPKC-inhibitor induced dextran accumulation could also be blocked by DMF (Figure 6 C,D). Therefore the sum

of these data reveal that TNF-α and loss of aPKC kinase activity lead to the induction of ST pyroptosis, most likely via a gasdermin-E mediated pathway.

Discussion:

The ST inhabits an exceptional anatomical position as a fetal-derived cell bathed in maternal blood at its apical surface but attached to the fetal compartment at its basal edge. Here we found that aPKC isoforms regulate the structure, permeability, and function of the ST apical surface in a spatially restricted manner. Additionally, we established that the pro-inflammatory cytokine TNF-α decreases ST aPKC-ι expression and profoundly alters ST apical structure and permeability, like disruption of aPKC isoforms, via the induction of pyroptosis. Therefore, our data suggests that aPKC isoforms are key regulators of ST homeostasis that can rapidly change in expression upon exposure to a pro-inflammatory stimulus leading to the release of a potent pro-inflammatory cytokine into maternal circulation.

Given the strong effects observed with the disruption of aPKC isoform expression and activity and that TNF-α leads to the isoform specific decrease in aPKC-ι expression it will be important to identify the relevant regulators controlling aPKCs within the ST. It is presently unknown whether aPKC isoforms function as a part of the Par-polarity complex in this cell type. Par-6 expression at the ST apical membrane from 12-weeks gestation has been shown(70), which coincides with the gestational age range we observed a significant signal accumulation for all aPKC isoforms at the apical surface (Figure 1), but the expression and localization of Par-3 within the ST is unknown. In

addition, isoform specific aPKC antibodies display a clear and consistent signal within the cytoplasm of the ST, suggesting that they may interact with other binding partners like p62/sequestrome, which is abundantly expressed in the ST(71). Our data revealed profound regional disruption of the apical F-actin cytoskeleton, but also the appearance of very large EEA1 positive vesicular structures in regions where F-actin was not visibly diminished. Therefore, there are likely multiple pathways through which aPKCs facilitate ST function that will need to be identified. Similarly, aPKC inhibitor treatment significantly decreased the ratio of activated to total ezrin as well as total ezrin signal (Figure 2), indicating that aPKC kinase activity could be directly phosphorylating ezrin at the Thr-567 residue as previously demonstrated(31), as well as indirectly controlling ezrin abundance via an additional pathway, to regulate ezrin homeostasis, microvillar structure, and maintenance. Intestinal cell regulation of aPKC-ι expression downstream of TNF-α is controlled by post-transcriptional mechanisms and ubiquitin-mediated degradation. Understanding how this is achieved in ST and whether other pro-inflammatory cytokines have similar effects will also be important in the future.

Our work also demonstrated that ST undergoes pyroptosis, most likely via a gasdermin-E mediated pathway. These results are consistent with multiple studies that have identified ST features by electron microscopy interpreted as regionalized necrosis(3, 19). These microvilli-replete ST regions have especially been identified in ST from preeclamptic pregnancies(19), where increased placental mature IL-β has also been reported(72). Placental mature-IL-1β was found to be predominantly produced by the ST(66) where the authors also observed a lack of cleaved-gasdermin-D signal, thereby

supporting our conclusions that ST pyroptosis is not mediated by gasdermin-D. Though, it is presently unclear how gasdermin-E cleavage is occurring since no detectable caspase-3 activation was seen in ST in our experiments. The lack of caspase-3 activation is consistent with previous literature showing that cleaved-caspase-3 is restricted to the cytotrophoblast progenitors *in vivo*(68). Granzyme family proteases have recently been shown to cleave gasdermin E (73, 74), but there is no evidence of their expression in the ST. Therefore, further elucidation of the ST pyroptotic cascade is necessary. In addition, DMF has a pleiotropic mechanism of action(75) and is likely working through multiple mechanisms to block ST pyroptosis in our system. Irrespective of the mechanism of action DMF clearly blocked the induction of permeability, without appreciable effects on the loss of apical F-actin signal induced by both TNF-α and aPKC inhibitor. Future work further examining its mechanism of action in the ST is warranted.

Our data showing that the release of IL-1β was not significantly altered by TNF-α treatment or aPKC inhibitor in term placental explants indicates that gestational-age dependent mechanisms blunting the release of pro-inflammatory factors from the ST may exist, despite a significant permeabilization of the ST to dextran. This is consistent with the observations of Megli *et al.* who found that constitutive NLRP3 inflammasome activation in the ST was significantly dampened at term compared to second trimester explants(66). It is presently unclear if TNF-α-induced pyroptosis requires further activation of the NLRP3 inflammasome above the constitutive baseline activity, or if it signals via an alternative inflammasome assembly. Elucidating additional pyroptotic-

initiating factors, and whether the mechanism of action has conserved regulatory points that could serve as therapeutic targets to block ST pyroptosis will also be an interesting future direction.

Finally, our work has clear implications for the pathobiology of placental disorders and infection during pregnancy. Presently there is no data that we are aware of examining aPKC isoform expression in the placentas from pregnancy complications. Our results revealed that disruption of aPKC isoforms induces the rapid appearance of features characteristic of regions of the ST from preeclamptic pregnancies. Though preeclampsia is defined by the onset of maternal hypertension after the 20th week of gestation and end organ failure(76-78), it is appreciated that the pathologic processes necessary for the development of the most severe form of the syndrome, early-onset preeclampsia, occur in early gestation(4). Interestingly, increased maternal first trimester circulating levels of IL-1β have been reported in pregnancies that go on to develop early-onset preeclampsia(79). Therefore, our data showing that pyroptosis can be initiated in 9-12 week placental samples suggest that chronic initiation of this pathway could contribute to the progression of some forms of preeclampsia and should be directly tested in the future. Increased maternal circulating levels of high mobility group box-1 (HMGB1) and ATP, which are known to be released from pyroptotic cells(59, 65), have also been observed in preeclampsia (80-84), though their role in the pathogenesis of the syndrome and the contribution of placental versus maternal cells to the increased levels remains to be elucidated.

Importantly, constitutive NLRP3 inflammasome activation has been shown to occur in the ST from ~20 weeks gestation on, thereby facilitating continuous IL-1β maturation and release(66). But Megli *et al.* also showed that IL-1β release from term placental explants was significantly decreased compared to mid-gestation explants which aligns with our data showing that TNF-α or aPKC inhibitor treatment induce robust permeabilization to dextran, but no significant IL-1β release from term placental explants (Figure 5). This suggests that pyroptotic ST may have gestational-age dependent secretory profiles, which could thereby elicit different responses from maternal cells. Alternatively, it is possible that pyroptosis in term ST proceeds through different mechanism than first trimester ST. Therefore, additional research to fully elucidate the complete pyroptotic cascade at different gestational ages will be an important direction to understand if anti-pyroptotic agents could be used to treat placental disorders such as preeclampsia in the future.

Materials and Methods:

Tissue collection

37-40 weeks gestation and first trimester human placental samples were collected by methods approved by the University of Alberta human research ethics board. Term placental tissue was collected after cesarean delivery without labour from uncomplicated pregnancies. First trimester placental tissue was obtained from elective pregnancy terminations following informed consent from the patients.

Floating placental explant culture and treatments

Placental samples were collected and rinsed in cold 1X phosphate-buffered saline (PBS) to remove blood. For term placentas, tissue was cut from three central cotyledons, decidua and blood clots were removed, and trimmed tissue was washed extensively in PBS to remove residual blood. For first trimester samples, placenta was identified, separated from decidua, blood clots were removed, and tissue was washed extensively in PBS to remove residual blood. Both first trimester and term tissue were then cut into uniform 2 mm^3 explants, placed into 48-well plates and incubated overnight at 37°C 5% CO_2 in Iscove's Modified Dulbecco's Medium (IMDM; Gibco) supplemented with 10% (v/v) Fetal Calf Serum (FCS; Multicell, Wisent Inc.) and penicillin streptomycin (5000 IU/mL; Multicell, Wisent Inc.). Following overnight incubation, explants were washed in serum-free IMDM with 0.1% (w/v) bovine serum albumin (BSA, Sigma-Aldrich) and incubated for 2-6hrs at 37°C 5% CO_2 +/- myristoylated aPKC pseudosubstrate inhibitor (5 μM; Invitrogen; Product number 77749) in IMDM+0.1% BSA. For TNF-α treatments, after washing in serum free medium, explants were pre-incubated for 30 min at 37 °C 5%CO_2 in IMDM +0.1% BSA, then medium was changed to IMDM +0.1% BSA +/- TNF-α (100 pg/mL or 10 ng/mL; Sigma-Aldrich) and incubated at 37°C 5% CO_2 for 6hrs. Explants were then washed with cold PBS and fixed with 4% paraformaldehyde for 2hrs on ice. For experiments performed with dimethyl fumarate (DMF; Sigma Aldrich), explants were washed as above, and then pre-incubated for 30 minute with solvent control (DMSO; 1:1000) or DMF (25μM). Medium was then changed and 100pg/mL TNF-α or 5 μM myristoylated aPKC pseudosubstrate inhibitor was added +/- DMF and incubated for 6hrs at 37°C 5% CO_2. Explants were then washed with cold

PBS and fixed with 4% paraformaldehyde for 2 hrs on ice. Technical triplicates were performed for all treatments.

siRNA Knockdown

siRNA knockdown was performed as previously reported(24). 9-12 week placental explants were placed into a 48-well plate with IMDM supplemented with 10% (v/v) FCS and gentamicin (50 µg/mL; Thermo Fischer Scientific). siRNA sequences targeting *PRKCI* (final concentration 0.2 nM; ON-TARGETplus siRNA J-040822-07-0020; Dharmacon) and *PRCKZ* (final concentration 0.2 nM; ON-TARGETplus siRNA J-003526-17-0010; Dharmacon), siRNA targeting both *PRKCI* and *PRCKZ,* or scrambled control (final concentration 0.2 nM; ON-TARGETplus Non-targeting Control Pool D-001810-10-20; Dharmacon) were added to the medium and incubated for 24hrs. After treatment, explants were washed with cold PBS before fixation with 4% paraformaldehyde for 2hrs on ice or collected in RIPA lysis buffer to perform western blotting.

Dextran Uptake Assay

Following in the last 30 minutes of treatment with aPKC inhibitor, TNF-α, or siRNA explants were incubated with 10,000 molecular weight (MW) neutral Dextran Texas Red™ (25 µg/mL; Invitrogen D1828) for 25 minutes in serum-free medium and washed with cold 1X phosphate buffered saline (PBS) before fixation with 4% paraformaldehyde for 2hrs on ice.

Transferrin endocytosis assay

Following aPKC inhibitor treatment, explants were incubated with fluorescently conjugated human transferrin-594 (CF 594; 25 µg/mL; Biotium) for 40 minutes. Explants were then washed extensively with cold 1X PBS and fixed in 4% paraformaldehyde for 2hrs on ice.

Primary trophoblast isolation, culture, and treatment

Term placental cytotrophoblasts were isolated according to previously published methods(24, 85). Briefly, placentas were trimmed of basal plate and decidual tissue, washed extensively to remove blood, minced, and digested via serial trypsin DNase digestion (Gibco). Following red blood cell lysis, immuno-elimination was performed with house-made columns using antibodies against CD9 (Clone TS9, Cell Sciences), MHC-class I (W6-32; Harlan-Sera Lab, Sussex UK), and MHC-class II (Clone 7H3). To obtain *in vitro* differentiated syncytiotrophoblasts, isolated cytotrophoblast progenitor cells were seeded into 6 well plates and cultured in IMDM+10%FCS+ Penicillin-streptomycin and incubated for 4hrs at 37°C 5%CO_2. Cells were then washed to remove non-adherent cells, medium changed to IMDM+10%FCS+Penicillin-streptomycin + 8-bromo-cAMP (10µm, Sigma-Aldrich), and then incubated overnight at 37°C 5%CO_2. Medium was changed to remove the 8-bromo-cAMP and the cells were incubated for a further 48hrs 37°C 5%CO_2 (72hrs in culture total).

TNF-α treatments were performed after differentiation into syncytiotrophoblasts. Medium was removed, cells were washed, and medium was replaced with IMDM+0.1%BSA and cells were incubated for 30 min at 37°C 5%CO_2. Medium was then changed to IMDM+0.1%BSA +/- TNF-α at the indicated doses for 4-12hrs. Cells were then washed, and protein lysates prepared for western blotting analysis.

Western Blotting

Samples were prepared by adding RIPA lysis buffer and protease inhibitor (1:100; Sigma Aldrich; P2714) to explants for 10 minutes before sonication and centrifugation at 14000 rpm for 14 minutes. Supernatant was collected for protein assay using a BCA Protein Assay. Protein was loaded and run on SDS-polyacrylamide gels before transfer onto nitrocellulose membranes. The membranes were blocked and probed with mouse anti-aPKC-ι (1:1000; BD Biosciences; 610207), rabbit anti-aPKC-ζ (1:2000; Atlas Antibodies; HPA021851), mouse anti-total aPKC (1:1000; Santa Cruz; sc-17781), rabbit anti-gasdermin E (1:10,000; Abcam; ab215191), mouse anti-AKT(pan) (1:2000; Cell Signaling Technology #2920), rabbit anti-phospho Ser473 AKT (1:2000; Cell Signaling Technology #4060), and mouse anti-β-actin (1:10000; Cell Signaling Technology #8457) and fluorescent secondary antibodies. Secondary antibodies included Alexa Fluor® donkey anti-mouse 680 (1:10,000; Invitrogen; A28183) and Alexa Fluor® donkey anti-rabbit 800 (1:10,000; Invitrogen; A21039). Following incubation, membranes were washed and visualized using a LI-COR Odyssey Infrared Scanner. For total protein quantification, membranes were stained using Fast-Green FCF (0.0001% Fast-Green FCF, 30% methanol, 7% acetic acid) for 15 minutes. Membranes were de-stained with

30% ethanol and 7% acetic acid before being washed with ddH_2O and scanning on the Licor scanner. Western blot quantitation was performed using the Licor Imaging Software and target protein band intensity was normalized to total protein.

Tissue staining and image analysis

Following fixation cultured explant or fixed non-cultured placental tissue was whole mount stained. Tissue was incubated with blocking buffer [5% normal donkey serum and 0.3% Triton x100, 1% human IgG (Invitrogen) in PBS] for 2hrs at room temperature. Blocking buffer was diluted 1:1 with PBS and explants were incubated with primary antibodies (anti-aPKC-ι; Atlas HPA025674); anti-aPKC-ζ (Atlas, HPA021851); anti-ezrin (Invitrogen; PA5-18541); anti-phospho Thr567 ezrin (Invitrogen; PA5-37763); anti β-actin (Cell Signaling Technologies; #8457); anti-EEA1 (R&D Systems MAB8047); anti-cleaved GSDMD Asp275 (Cell Signaling Technologies #36425); anti-GSDME (Santa Cruz Biotechnology; sc393162); anti-cleaved caspase-3 Asp175 (Cell Signaling Technologies; #9661) anti-E-cadherin (R&D Systems; MAB18381) or biotinylated-WGA Lectin (Vector Biolabs). Then washed and incubated with the appropriate secondary antibodies (Alexa Fluor™, Invitrogen) and/or fluorescently conjugated phalloidin (1:400; iFluor 405 or iFluor594; AAT Bioquest). Hoechst 33342 (Invitrogen) was then added for 30 mins. Tissue was then washed with PBS-Tween and PBS before being mounted with imaging spacers.

All images were captured with a Zeiss LSM 700 confocal microscope using a Zeiss 20x/0.8 M27 lens or a Zeiss 63x/1.4 Oil DIC M27 lens. 10-15 μm Z-stack images with a 1 μm

step-size were captured at 63x magnification. Three images per treatment were captured. Image capture was restricted to blunt-ended terminal projections of the placental villi from first trimester and term samples.

Image quantitation

All image quantitation was performed with Volocity Imaging software (Version 6.3; Quorum Technologies).

Co-localization analyses- Triplicate regions of interest of the ST apical surface were selected using the freehand tool for each image, and average global Pearson's correlation coefficient for each region of interest was determined for transferrin:EEA-1 colocalization or the anti-aPKC-ι or anti-aPKC-ζ signal and anti-ezrin signal.

Apical phalloidin intensity- Triplicate regions of interest were manually selected from the ST apical surface for each image, and average mean signal intensity of the phalloidin signal for each region of interest was determined.

Dextran uptake-Total villous volume was isolated as a region of interest for each image. Total sum dextran signal was normalized to the total volume of the region of interest. To determine the sum dextran signal/volume.

Scanning electron microscopy

After treatment in culture, triplicate explants from each treatment group were collected and fixed in EM fixative (2.5% Glutaraldehyde; 2% Paraformaldehyde in 0.1 M Phosphate Buffer). Samples were then washed 3 times with 0.1 M Phosphate Buffer,

dehydrated through a graded ethanol series, serially washed, then incubated in a graded series of increasing Hexamethyldisilazane (HMDS) and decreasing ethanol concentration. Once equilibrated with 100% HMDS, they were left to dry overnight. The samples were then mounted and sputter coated with Au/Pd (Hummer 6.2 Sputter Coater, Anatech) the next day and images were captured with a Zeiss EVO10 SEM microscope using SmartSEM software (Version 6.06).

Transmission electron microscopy

After treatment in culture, triplicate explants from each treatment group were collected and fixed in EM fixative (2.5% Glutaraldehyde; 2% Paraformaldehyde in 0.1 M Phosphate Buffer). Samples were washed with 0.1 M Phosphate Buffer, then fixed and stained in 1% Osmium tetroxide for 1 hour. The samples were then washed and dehydrated via a graded ethanol series. Dehydrated samples were left overnight in a 1:1 Ethanol:Spurr Resin mix. The following day, the samples were incubated with fresh spurr resin, embedded in resin and cured overnight in a 70°C oven. The cured sample blocks were then cut in 70-90nm sections using an ultramicrotome (Reichert-Jung Ultracut_E Ultramicrotome). Sections were stained with urnayl acetate and lead citrate on grids and viewed under light microscope to make sure that the cut sections had tissue. Finally the grids were used to image the samples with a Philips/FEI (Morgagni) TEM, and Digital Micrograph software (Version 1.81.78).

ELISA assays

Conditioned explant culture medium was collected from technical triplicates after 6hrs incubation with treatments and centrifuged at 12,000 rpm for 10 minutes and the supernatant aliquoted then stored at -20℃. Explant tissue was washed with PBS then flash frozen and stored at -80℃ until total protein was extracted and determined by BCA assay, as above. ELISAs were performed using a β-HCG ELISA kit (DRG International EIA-1911) and IL-1β ELISA kit (DY401-05, R&D systems). Plates were read using the Biotek Synergy HTX plate reader (Gen 5 software). The β-HCG and IL-1β values were interpolated using GraphPad PRISM 9 (Version 9.3.1) and normalized to the total protein from the explant the medium was produced by.

Statistical Analysis

Statistical analyses were completed using GraphPad PRISM 9 (Version 9.3.1.) with an α= 0.05 as the threshold for significance. Exact statistical methods used for individual experiments are contained in the figure legends. All graphs represent mean+/- S.E.M.

Acknowledgements:

We would like to thank Dr. Carolyn Jones for her feedback on the initial data and Maya Henriquez for the collection of placental tissue and all the families that donated tissue for the study. We would also like to thank Dr. Kacie Norton and Arlene Oatway of the University of Alberta Biological Sciences Imaging Facility for their expert technical advice for the electron microscopy sample preparation and imaging. This work was supported by funding from the Canadian Institutes of Health Research (MRC-167968) as well as the Women and Children's Health Research Institute and their generous donors: the Alberta

Women's Health Foundation and the Stollery Children's Hospital Foundation. K.P. was supported by the MaTCH program stipend award. S.S is supported by an Alberta-Innovates Graduate Studentship. J.N. was supported by summer studentships from the Women and Children's Health Research Institute, Alberta-Innovates, and NSERC.

Author Contributions:

K.P, J.N, S.S, A.Z., and M.R performed experiments, analyzed data, and contributed to the writing and editing of the manuscript. M.R. obtained funding and conceptualized the project.

References:

1. G. J. M. D. D. F. Burton, E. M. D. P. Jauniaux, What is the placenta? *American Journal of Obstetrics and Gynecology* **213**, S6.e4 (2015).
2. K. Benirschke (2000) Pathology of the human placenta. ed P. Kaufmann (Springer, New York :).
3. H. Fox, A. Agrafojo-Blanco, Scanning electron microscopy of the human placenta in normal and abnormal pregnancies. *Eur J Obstet Gynecol Reprod Biol* **4**, 45-50 (1974).
4. A. C. Staff, The two-stage placental model of preeclampsia: An update. *J Reprod Immunol* **134-135**, 1-10 (2019).
5. C. W. G. Redman, A. C. Staff, J. M. Roberts, Syncytiotrophoblast stress in preeclampsia: the convergence point for multiple pathways. *Am J Obstet Gynecol* **226**, S907-S927 (2022).
6. G. J. Burton, E. Jauniaux, Pathophysiology of placental-derived fetal growth restriction. *Am J Obstet Gynecol* **218**, S745-S761 (2018).
7. R. G. Fehon, A. I. McClatchey, A. Bretscher, Organizing the cell cortex: the role of ERM proteins. *Nat Rev Mol Cell Biol* **11**, 276-287 (2010).
8. T. Pelaseyed, A. Bretscher, Regulation of actin-based apical structures on epithelial cells. *J Cell Sci* **131** (2018).
9. R. Viswanatha, P. Y. Ohouo, M. B. Smolka, A. Bretscher, Local phosphocycling mediated by LOK/SLK restricts ezrin function to the apical aspect of epithelial cells. *J Cell Biol* **199**, 969-984 (2012).

10. L. Zhu *et al.*, High turnover of ezrin T567 phosphorylation: conformation, activity, and cellular function. *Am J Physiol Cell Physiol* **293**, C874-884 (2007).

11. R. Davies *et al.*, Microvillous tip vesicles may be an origin of placental extracellular vesicles. *Placenta* **123**, 24-30 (2022).

12. A. I. Ivanov, A. Nusrat, C. A. Parkos, Endocytosis of epithelial apical junctional proteins by a clathrin-mediated pathway into a unique storage compartment. *Mol Biol Cell* **15**, 176-188 (2004).

13. K. Schneeberger, S. Roth, E. E. S. Nieuwenhuis, S. Middendorp (2018) Intestinal epithelial cell polarity defects in disease: lessons from microvillus inclusion disease. (The Company of Biologists, England), p dmm031088.

14. R. Halaoui *et al.*, Progressive polarity loss and luminal collapse disrupt tissue organization in carcinoma. *Genes Dev* **31**, 1573-1587 (2017).

15. K. D. Walton, A. M. Freddo, S. Wang, D. L. Gumucio, Generation of intestinal surface: an absorbing tale. *Development* **143**, 2261-2272 (2016).

16. B. S. Holder, C. L. Tower, C. J. Jones, J. D. Aplin, V. M. Abrahams, Heightened pro-inflammatory effect of preeclamptic placental microvesicles on peripheral blood immune cells in humans. *Biol Reprod* **86**, 103 (2012).

17. I. de Luca Brunori *et al.*, Placental barrier breakage in preeclampsia: ultrastructural evidence. *Eur J Obstet Gynecol Reprod Biol* **118**, 182-189 (2005).

18. M. Battistelli *et al.*, Ultrastructural study on human placenta from intrauterine growth retardation cases. *Microscopy Research and Technique* **65**, 150-158 (2004).

19. C. J. P. Jones, H. Fox, An ultrastructural and ultrahistochemical study of the human placenta in maternal pre-eclampsia. *Placenta* **1**, 61-76 (1980).

20. A. Román-Fernández, D. M. Bryant, Complex Polarity: Building Multicellular Tissues Through Apical Membrane Traffic. *Traffic* **17**, 1244-1261 (2016).

21. D. Lin *et al.*, A mammalian PAR-3-PAR-6 complex implicated in Cdc42/Rac1 and aPKC signalling and cell polarity. *Nat Cell Biol* **2**, 540-547 (2000).

22. Y. Hong, aPKC: the Kinase that Phosphorylates Cell Polarity. *F1000Res* **7** (2018).

23. C. Gerri *et al.*, Initiation of a conserved trophectoderm program in human, cow and mouse embryos. *Nature* 10.1038/s41586-020-2759-x (2020).

24. S. Shaha *et al.*, Human placenta and trophoblasts simultaneously express three isoforms of atypical protein kinase-c. *Placenta* **119**, 39-43 (2022).

25. L. A. Lopez-Garcia *et al.*, Allosteric regulation of protein kinase PKCzeta by the N-terminal C1 domain and small compounds to the PIF-pocket. *Chem Biol* **18**, 1463-1473 (2011).

26. I. S. Tobias, A. C. Newton, Protein Scaffolds Control Localized Protein Kinase Czeta Activity. *J Biol Chem* **291**, 13809-13822 (2016).

27. S. Seidl *et al.*, Phenotypical analysis of atypical PKCs in vivo function display a compensatory system at mouse embryonic day 7.5. *PLoS One* **8**, e62756 (2013).

28. M. Leitges *et al.*, Targeted disruption of the zetaPKC gene results in the impairment of the NF-kappaB pathway. *Mol Cell* **8**, 771-780 (2001).

29. B. Bhattacharya *et al.*, Atypical protein kinase C iota (PKClambda/iota) ensures mammalian development by establishing the maternal-fetal exchange interface. *Proc Natl Acad Sci U S A* **117**, 14280-14291 (2020).

30. R. S. Soloff, C. Katayama, M. Y. Lin, J. R. Feramisco, S. M. Hedrick, Targeted deletion of protein kinase C lambda reveals a distribution of functions between the two atypical protein kinase C isoforms. *J Immunol* **173**, 3250-3260 (2004).

31. F. A. Wald *et al.*, Atypical protein kinase C (iota) activates ezrin in the apical domain of intestinal epithelial cells. *J Cell Sci* **121**, 644-654 (2008).

32. M. Berryman, R. Gary, A. Bretscher, Ezrin oligomers are major cytoskeletal components of placental microvilli: a proposal for their involvement in cortical morphogenesis. *J Cell Biol* **131**, 1231-1242 (1995).

33. C. L. Crespo *et al.*, The PAR complex controls the spatiotemporal dynamics of F-actin and the MTOC in directionally migrating leukocytes. *J Cell Sci* **127**, 4381-4395 (2014).

34. H. Zhang, I. G. Macara, The PAR-6 polarity protein regulates dendritic spine morphogenesis through p190 RhoGAP and the Rho GTPase. *Dev Cell* **14**, 216-226 (2008).

35. M. Georgiou, E. Marinari, J. Burden, B. Baum, Cdc42, Par6, and aPKC regulate Arp2/3-mediated endocytosis to control local adherens junction stability. *Curr Biol* **18**, 1631-1638 (2008).

36. Y. Hong, aPKC: the Kinase that Phosphorylates Cell Polarity. *F1000Research* **7**, 903 (2018).

37. A. Elbediwy *et al.*, The Rho family GEF FARP2 is activated by aPKCiota to control tight junction formation and polarity. *J Cell Sci* **132** (2019).

38. M. Riddell *et al.*, aPKC controls endothelial growth by modulating c-Myc via FoxO1 DNA-binding ability. *Nat Commun* **9**, 5357 (2018).

39. P. J. Parker, V. Justilien, P. Riou, M. Linch, A. P. Fields, Atypical protein kinase Ciota as a human oncogene and therapeutic target. *Biochem Pharmacol* **88**, 1-11 (2014).

40. G. Michaux *et al.*, The localisation of the apical Par/Cdc42 polarity module is specifically affected in microvillus inclusion disease. *Biol Cell* **108**, 19-28 (2016).

41. F. A. Wald *et al.*, Aberrant expression of the polarity complex atypical PKC and non-muscle myosin IIA in active and inactive inflammatory bowel disease. *Virchows Arch* **459**, 331-338 (2011).

42. A. Mashukova, F. A. Wald, P. J. Salas, Tumor necrosis factor alpha and inflammation disrupt the polarity complex in intestinal epithelial cells by a posttranslational mechanism. *Mol Cell Biol* **31**, 756-765 (2011).

43. R. Raghupathy, Cytokines as key players in the pathophysiology of preeclampsia. *Med Princ Pract* **22 Suppl 1**, 8-19 (2013).

44. N. S. Sunderland *et al.*, Tumor necrosis factor alpha induces a model of preeclampsia in pregnant baboons (Papio hamadryas). *Cytokine* **56**, 192-199 (2011).

45. B. T. Alexander, K. L. Cockrell, M. B. Massey, W. A. Bennett, J. P. Granger, Tumor necrosis factor-alpha-induced hypertension in pregnant rats results in

decreased renal neuronal nitric oxide synthase expression. *Am J Hypertens* **15**, 170-175 (2002).

46. T. Cotechini *et al.*, Inflammation in rat pregnancy inhibits spiral artery remodeling leading to fetal growth restriction and features of preeclampsia. *J Exp Med* **211**, 165-179 (2014).

47. P. A. Carpentier, A. L. Dingman, T. D. Palmer, Placental TNF-alpha signaling in illness-induced complications of pregnancy. *Am J Pathol* **178**, 2802-2810 (2011).

48. T. Li-Chun Lisa *et al.* (2015) Zeta Inhibitory Peptide Disrupts Electrostatic Interactions That Maintain Atypical Protein Kinase C in Its Active Conformation on the Scaffold p62. (American Society for Biochemistry and Molecular Biology, United States), pp 21845-21856.

49. M. Shigenori, S. Koji, K.-n. Midori, T. Tetsuhiko, T. Shoji, Fluid shear triggers microvilli formation via mechanosensitive activation of TRPV6. *Nature Communications* **6**, 8871 (2015).

50. K. Forbes, M. Desforges, R. Garside, J. D. Aplin, M. Westwood, Methods for siRNA-mediated reduction of mRNA and protein expression in human placental explants, isolated primary cells and cell lines. *Placenta* **30**, 124-129 (2009).

51. E. Sgambati, R. Biagiotti, M. Marini, E. Brizzi, Lectin histochemistry in the human placenta of pregnancies complicated by intrauterine growth retardation based on absent or reversed diastolic flow. *Placenta* **23**, 503-515 (2002).

52. M. C. Lee, I. Damjanov, Lectin histochemistry of human placenta. *Differentiation* **28**, 123-128 (1984).

53. X. Shao *et al.*, Placental trophoblast syncytialization potentiates macropinocytosis via mTOR signaling to adapt to reduced amino acid supply. *Proc Natl Acad Sci U S A* **118** (2021).

54. T. Spence *et al.*, Maternal Serum Cytokine Concentrations in Healthy Pregnancy and Preeclampsia. *J Pregnancy* **2021**, 6649608 (2021).

55. M. Kim, A. Datta, P. Brakeman, W. Yu, K. E. Mostov, Polarity proteins PAR6 and aPKC regulate cell death through GSK-3beta in 3D epithelial morphogenesis. *J Cell Sci* **120**, 2309-2317 (2007).

56. W. S. Ratnayake, A. H. Apostolatos, D. A. Ostrov, M. Acevedo-Duncan, Two novel atypical PKC inhibitors; ACPD and DNDA effectively mitigate cell proliferation and epithelial to mesenchymal transition of metastatic melanoma while inducing apoptosis. *Int J Oncol* **51**, 1370-1382 (2017).

57. J. D. Webster, D. Vucic, The Balance of TNF Mediated Pathways Regulates Inflammatory Cell Death Signaling in Healthy and Diseased Tissues. *Front Cell Dev Biol* **8**, 365 (2020).

58. O. Micheau, J. Tschopp, Induction of TNF receptor I-mediated apoptosis via two sequential signaling complexes. *Cell* **114**, 181-190 (2003).

59. P. Yu *et al.*, Pyroptosis: mechanisms and diseases. *Signal Transduct Target Ther* **6**, 128 (2021).

60. J. Hou *et al.*, PD-L1-mediated gasdermin C expression switches apoptosis to pyroptosis in cancer cells and facilitates tumour necrosis. *Nat Cell Biol* **22**, 1264-1275 (2020).

61. Y. Wang *et al.*, Chemotherapy drugs induce pyroptosis through caspase-3 cleavage of a gasdermin. *Nature* **547**, 99-103 (2017).

62. S. B. Kovacs, E. A. Miao, Gasdermins: Effectors of Pyroptosis. *Trends Cell Biol* **27**, 673-684 (2017).

63. E. De Schutter *et al.*, Plasma membrane perforation by GSDME during apoptosis-driven secondary necrosis. *Cell Mol Life Sci* **79**, 19 (2021).

64. B. Zhou, D. W. Abbott, Gasdermin E permits interleukin-1 beta release in distinct sublytic and pyroptotic phases. *Cell Rep* **35**, 108998 (2021).

65. A. Volchuk, A. Ye, L. Chi, B. E. Steinberg, N. M. Goldenberg, Indirect regulation of HMGB1 release by gasdermin D. *Nat Commun* **11**, 4561 (2020).

66. C. Megli, S. Morosky, D. Rajasundaram, C. B. Coyne, Inflammasome signaling in human placental trophoblasts regulates immune defense against Listeria monocytogenes infection. *J Exp Med* **218** (2021).

67. C. Rogers *et al.*, Cleavage of DFNA5 by caspase-3 during apoptosis mediates progression to secondary necrotic/pyroptotic cell death. *Nat Commun* **8**, 14128 (2017).

68. M. S. Longtine, B. Chen, A. O. Odibo, Y. Zhong, D. M. Nelson, Caspase-mediated apoptosis of trophoblasts in term human placental villi is restricted to cytotrophoblasts and absent from the multinucleated syncytiotrophoblast. *Reproduction* **143**, 107-121 (2012).

69. F. Humphries *et al.*, Succination inactivates gasdermin D and blocks pyroptosis. *Science* **369**, 1633-1637 (2020).

70. T. Sivasubramaniyam *et al.*, Where polarity meets fusion: role of Par6 in trophoblast differentiation during placental development and preeclampsia. *Endocrinology* **154**, 1296-1309 (2013).

71. Y. J. Pan *et al.*, Expression of urotensin II is associated with placental autophagy in patients with severe preeclampsia. *J Hum Hypertens* **32**, 759-769 (2018).

72. S. B. Cheng *et al.*, Pyroptosis is a critical inflammatory pathway in the placenta from early onset preeclampsia and in human trophoblasts exposed to hypoxia and endoplasmic reticulum stressors. *Cell Death Dis* **10**, 927 (2019).

73. Z. Zhang *et al.*, Gasdermin E suppresses tumour growth by activating anti-tumour immunity. *Nature* **579**, 415-420 (2020).

74. Z. Zhou *et al.*, Granzyme A from cytotoxic lymphocytes cleaves GSDMB to trigger pyroptosis in target cells. *Science* **368** (2020).

75. J. Bruck, R. Dringen, A. Amasuno, I. Pau-Charles, K. Ghoreschi, A review of the mechanisms of action of dimethylfumarate in the treatment of psoriasis. *Exp Dermatol* **27**, 611-624 (2018).

76. E. Phipps, D. Prasanna, W. Brima, B. Jim, Preeclampsia: Updates in Pathogenesis, Definitions, and Guidelines. *Clin J Am Soc Nephrol* **11**, 1102-1113 (2016).

77. A. L. Tranquilli, M. A. Brown, G. G. Zeeman, G. Dekker, B. M. Sibai, The definition of severe and early-onset preeclampsia. Statements from the International Society for the Study of Hypertension in Pregnancy (ISSHP). *Pregnancy Hypertens* **3**, 44-47 (2013).

78. A. L. Tranquilli *et al.*, The classification, diagnosis and management of the hypertensive disorders of pregnancy: A revised statement from the ISSHP. *Pregnancy Hypertension: An International Journal of Women's Cardiovascular Health* **4**, 97-104 (2014).

79. J. E. Siljee *et al.*, Identification of interleukin-1 beta, but no other inflammatory proteins, as an early onset pre-eclampsia biomarker in first trimester serum by bead-based multiplexed immunoassays. *Prenat Diagn* **33**, 1183-1188 (2013).

80. M. E. Brien *et al.*, Alarmins at the maternal-fetal interface: involvement of inflammation in placental dysfunction and pregnancy complications (1). *Can J Physiol Pharmacol* **97**, 206-212 (2019).

81. F. Spaans, P. de Vos, W. W. Bakker, H. van Goor, M. M. Faas, Danger signals from ATP and adenosine in pregnancy and preeclampsia. *Hypertension* **63**, 1154-1160 (2014).

82. W. W. Bakker *et al.*, Plasma hemopexin activity in pregnancy and preeclampsia. *Hypertens Pregnancy* **26**, 227-239 (2007).

83. V. Wairachpanich, V. Phupong, Second-trimester serum high mobility group box-1 and uterine artery Doppler to predict preeclampsia. *Sci Rep* **12**, 6886 (2022).

84. Y. Hu *et al.*, High-Mobility Group Box 1 From Hypoxic Trophoblasts Promotes Endothelial Microparticle Production and Thrombophilia in Preeclampsia. *Arterioscler Thromb Vasc Biol* **38**, 1381-1391 (2018).

85. L. J. Guilbert *et al.*, Preparation and functional characterization of villous cytotrophoblasts free of syncytial fragments. *Placenta* **23**, 175-183 (2002).

Figure Legends:

Figure 1: aPKC-ι and aPKC-ζ strongly colocalize with ezrin at the ST apical surface in 9-12 weeks and 37-40 week placental ST. A) Representative images of 9-12 week (top panel) and 37-40 week (bottom panel) placenta tissue stained with anti-aPKC-ι (green), anti-ezrin (magenta) and anti β-actin (blue); left panel=zy plane, scale bar=10μm; right panel=xy plane; arrow heads=ST apical surface; single image plane of z-stack images; B) Summary data for quantitation of aPKC-ι and ezrin Pearson's colocalization coefficient at the apical ST through varying gestational ages; *n*=3; *=p<0.05; **=p<0.01, ***=p<0.001; bold dashed line=median; C) Representative images of 9-12 week (top panel) and 37-40 week (bottom panel) placental explants stained with anti-aPKC-ζ (green), anti-Ezrin (magenta) and anti β-actin (blue); left panel=zy plane, scale bar=10μm; right panel=xy plane; arrow heads=ST apical surface; single image plane of z-stack images; D) Summary data for quantitation of ST apical aPKC-ζ and ezrin Pearson's colocalization coefficient through varying gestational ages; *n*=3; *=p<0.05; **=p<0.01; bold dashed line=median; All analyses performed with one-way ANOVA with Tukey's post-hoc test.

Figure 2: Loss of aPKC kinase activity or expression alters apical ezrin activation and abundance and F-actin. A) Representative images of 9-12 week placental explants treated +/- aPKC inhibitor for 6hrs stained for anti-phospho(Thr567)-ezrin (green), anti-ezrin (magenta) and anti-β-actin (blue); left panel=zy plane, scale bar=10μm; right panel=xy plane; single image plane of z-stack images; B) Summary data for quantitation of ST apical ezrin signal intensity in 9-12 week explants; *n*=5; *=p<0.05; C) Summary data for quantitation of ST apical phospho(Thr567) ezrin relative

to total ezrin signal intensity in 9-12 week explants; *n*=5; *=p<0.05; D) Summary data for quantitation of ST apical ezrin signal intensity in 37-40 week explants; *n*=3; *=p<0.05; **=p<0.01; E) Summary data for quantitation of ST apical phospho(Thr567) ezrin relative to total ezrin signal intensity in 37-40 week explants; *n*=3; *=p<0.05; F) Representative images of 9-12 week placental explants treated +/- aPKC inhibitor for 6hrs stained with phalloidin (green) and Hoechst-33342 (blue); left panel=zy plane, scale bar=10μm; right panel=xy plane; single image plane of z-stack images; G) Summary data for quantitation of ST apical phalloidin signal intensity in 9-12 week explants; *n*=4; ***=p<0.001; H) Summary data for quantitation of ST apical phalloidin signal intensity in 37-40 week explants; *n*=3; **=p<0.01; All above analyses performed using one-sample t-test; summary graphs mean +/- S.E.M; I) Representative western blot with anti-aPKC-ι and anti-β-actin following siRNA knockdown targeting *PRKCI*; J) Representative western blot with anti-aPKC-ζ and anti-β-actin following siRNA knockdown targeting *PRKCZ*; K) Representative western blot with anti-total-aPKC and anti-β-actin following siRNA knockdown targeting *PRKCI* and *PRKCZ*; L) Summary data for quantitation of relative aPKC-ι expression following siRNA knockdown targeting *PRKCI*; *n*=4; *=p<0.05; Student's t-test; M) Summary data for quantitation of relative aPKC-ζ expression following siRNA knockdown targeting *PRKCZ*; *n*=4; *=p<0.05; Student's t-test; N) Summary data for quantitation of relative aPKC-ζ III expression following siRNA knockdown targeting *PRKCZ*; *n*=4; *=p<0.05; Student's t-test; O) Summary data for quantitation of relative total aPKC expression following siRNA knockdown targeting *PRKCI* and *PRKCZ*; *n*=4; *=p<0.05; Student's t-test; P) Summary data for quantitation of relative aPKC-ζ III expression following siRNA knockdown

targeting *PRKCI* and *PRKCZ*; *n*=4; *=p<0.05; Student's t-test; Q) Representative images of 9-12 week placental explants treated with isoform specific siRNA for 24 hrs and stained with phalloidin (green) and WGA lectin (magenta); left panel=zy plane, scale bar=10μM; right panel=xy plane; single image plane of z-stack images; R) Summary data for quantitation of ST apical phalloidin signal intensity in 9-12 week explants treated with aPKC isoform specific siRNA; *n*=3; ****=p<0.0001; Analysis performed using one-way ANOVA with Dunnett's post-hoc test; summary graphs mean +/- S.E.M.

Figure 3: aPKC inhibition leads to ST apical membrane simplification, decreased microvilli and cytoplasmic density, permeabilization of ST, and alteration of ST endocytic trafficking. A) Representative SEM images of 9-12 week placental explants treated with aPKC inhibitor for 6hrs (representative of *n*=3); right panels=isolated zoomed images of boxed area indicated on left; B) Representative TEM images of 9-12 week placental explants treated +/- aPKC inhibitor for 6hrs (representative of *n*=3); C) Representative images of 9-12 week placental explants after 10,000 MW dextran-Texas Red uptake (green) and phalloidin staining (magenta) following 2hrs treatment with aPKC inhibitor; left panels=merged image; right panels=isolated dextran signal; single plane of z-stack images; D) Summary data for quantitation of sum of 10,000 MW dextran-Texas Red per μm^3 in 9-12 week placental explants after 2hrs aPKC inhibitor treatment; *n*=4; *=p<0.05; Student's t-test; E) Representative images of 9-12 week placental explants after 10,000 MW dextran-Texas Red uptake (green) and phalloidin staining (magenta) following 24hrs treatment with scramble control or siRNA sequences targeting *PRKCI* and/or *PRKCZ*; top panels=merged image; bottom panels=isolated

dextran signal; single image plane of z-stack images; F) Summary data for quantitation of sum of 10,000 MW dextran-Texas Red per μm^3 in 9-12 week placental explants following siRNA knockdown of *PRKCI* and/or *PRKCZ*; *n*=3; *=p<0.05, **=p<0.01; one-way ANOVA with Dunnett's post-hoc test; G) Representative images of EEA-1 (green), transferrin-594 (magenta), and phalloidin (blue) staining in 9-12 week placental explants after 2hrs aPKC inhibitor treatment; top panels=control; bottom panels=aPKC inhibitor; right panels=isolated EEA1 signal; single plane of z-stack image H) Summary data for quantitation of global Pearsons correlation coefficient for EEA1:transferrin colocalization in 9-12 week placental explants; *n*=4; **=p<0.01; Student's t-test; I) Summary data for quantitation of β-hCG concentration normalized to total protein levels in placental explant medium following aPKC inhibitor treatment; *n*=3, *=p<0.05; Student's t-test; All summary graphs mean +/- S.E.M.

Figure 4: TNF-α leads to dose dependent isoform specific decrease in aPKC-ι expression, loss of apical F-actin, and permeabilization of ST. A) Representative western blot analyses of *in vitro* differentiated primary ST treated for 4hrs with indicated doses of TNF-α, immunoblotted with anti-aPKC-ι, anti-aPKC-ζ, and anti-β-actin; B) Western blot quantitation for aPKC-ι; C) Western blot quantitation for aPKC-ζ (70kDa form); D) Western blot quantitation for aPKC-ζ III (55kDa form); *n*=4 patient derived cells; **=p<0.01; ***=p<0.001; E) Representative images of 9-12 week placental explants treated with indicated doses of TNF-α for 6hrs and stained with phalloidin (green) and WGA lectin (magenta); top panels=merged image; bottom panels= isolated phalloidin; left panel=zy plane, scale bar=10μm; right panel=xy plane; single image plane of z-stack images; F) Summary data for quantitation of ST apical phalloidin signal

intensity in 9-12 week explants; *n*=4; *=p<0.05; **=p<0.01; G) Summary data for quantitation of ST apical phalloidin signal intensity in 37-40 week explants; *n*=4; ***=p<0.001; H) Representative SEM images of 37-40 week explants +/- 100 pg/mL TNF-α for 6hrs; right panels= higher magnification images of the same samples; *n*=4; (I) Representative images of 10,000 MW dextran-Texas Red (green) uptake and phalloidin (magenta) staining in 37-40 week placental explants after 6hrs treatment with indicated doses of TNF-α; top panels=merged image; bottom panels=isolated dextran; single plane image of z-stack (J) Summary data for quantitation of sum dextran signal per μm^3 in the ST of 37-40 week placental explants; *n*=3; **=p<0.01; (K) Summary data for quantitation of sum dextran signal per μm^3 in the ST of 9-12 week placental explants; *n*=3; *=p<0.05; ***=p<0.001; All analyses one-way ANOVA with Dunnett's post-hoc test; summary graphs mean +/- S.E.M.

Figure 5: TNF-α leads to the induction of ST pyroptosis via gasdermin-E cleavage. A) IL-1β in 9-12 week placental explant medium after 6hr 100pg/mL TNF-α stimulation; *n*=3; *=p<0.05; one-factor t-test; B) IL-1β in 9-12 week placental explant medium after 6hr aPKC inhibitor treatment; *n*=3; one-factor t-test *=p<0.05; C) IL-1β in 37-40 week placental explant medium after 6hr 100pg/mL TNF-α stimulation; *n*=6; one-factor t-test; D) IL-1β in 37-40 week placental explant medium after 6hr aPKC inhibitor treatment; *n*=4; one-factor t-test; E) Representative image of anti-cleaved gasdermin D (cl-GSDMD, magenta); anti-E-cadherin (green), and Hoescht 33342 stained 37-40 week placental explants +/- 100pg/mL TNF-α for 6hrs; bottom panels= higher magnification images of indicated areas; F) Representative images of anti-gasdermin E (GSDME,

green), 10,000 MW dextran-Texas Red (magenta), and phalloidin (blue) in 9-12 week placental explants treated +/- 100pg/mL TNF-α for 6hrs; left panel=yz single image plane of merged image scale bar=10μm; center panel= xy single image plane of merged image; right panel= gasdermin E alone xy single image plane; G) Representative images of anti-gasdermin E (GSDME, green), 10,000 MW dextran-Texas Red uptake (magenta), and phalloidin (blue) in 37-40 week placental explants treated +/- 100pg/mL TNF-α for 6hrs; left panel=yz single image plane of merged image; scale bar=10μm; center panel=xy single image plane of merged image; right panel= gasdermin E alone; xy single image plane; H) Representative western blot of *in vitro* differentiated primary ST treated +/- 10ng/mL TNF-α for 12 hrs; I) Quantitation of western blot analyses for gasdermin E p30 normalized to total protein; *n*=3 experimental replicates from *n*=2 patient derived cells; *=p<0.05; one-factor t-test; J) Representative images of anti-cleaved caspase 3 (cl-Casp3, green), anti-E-cadherin (magenta), and Hoescht 33342 stained 37-40 week placental explants +/- 100pg/mL TNF-α for 6hrs; K) Representative images of anti-cleaved caspase 3 (cl-Casp3, green), anti-E-cadherin (magenta), and Hoescht 33342 stained 9-12 week placental explants +/- 100pg/mL TNF-α for 6hrs; All graphs mean +/- S.E.M.

Figure 6: DMF treatment blocks TNF-α induced ST permeability and IL-1β release. A) Representative images of 10,000 MW dextran-Texas Red (magenta) uptake and phalloidin (green) staining in 9-12 week placental explants after 6hrs treatment +/- DMF, 100pg/mL TNF-α, or both; B) Summary data for quantitation of sum dextran signal per μm^3 in the ST of 9-12 week placental explants; *n*=4; *=p<0.05, **=p<0.01; one-way ANOVA Sidak's multiple comparison test; C) Representative images of 10,000 MW

dextran-Texas Red uptake (magenta) and phalloidin (green) staining in 9-12 week placental explants after 6hrs treatment +/- DMF, aPKC inhibitor, or both; D) Summary data for quantitation of sum dextran signal per μm^3 in the ST of 9-12 week placental explants; *n*=3; *=p<0.05; **=p<0.01; one-way ANOVA with Sidak's multiple comparison test; All graphs mean +/- S.E.M.

Figure 1:

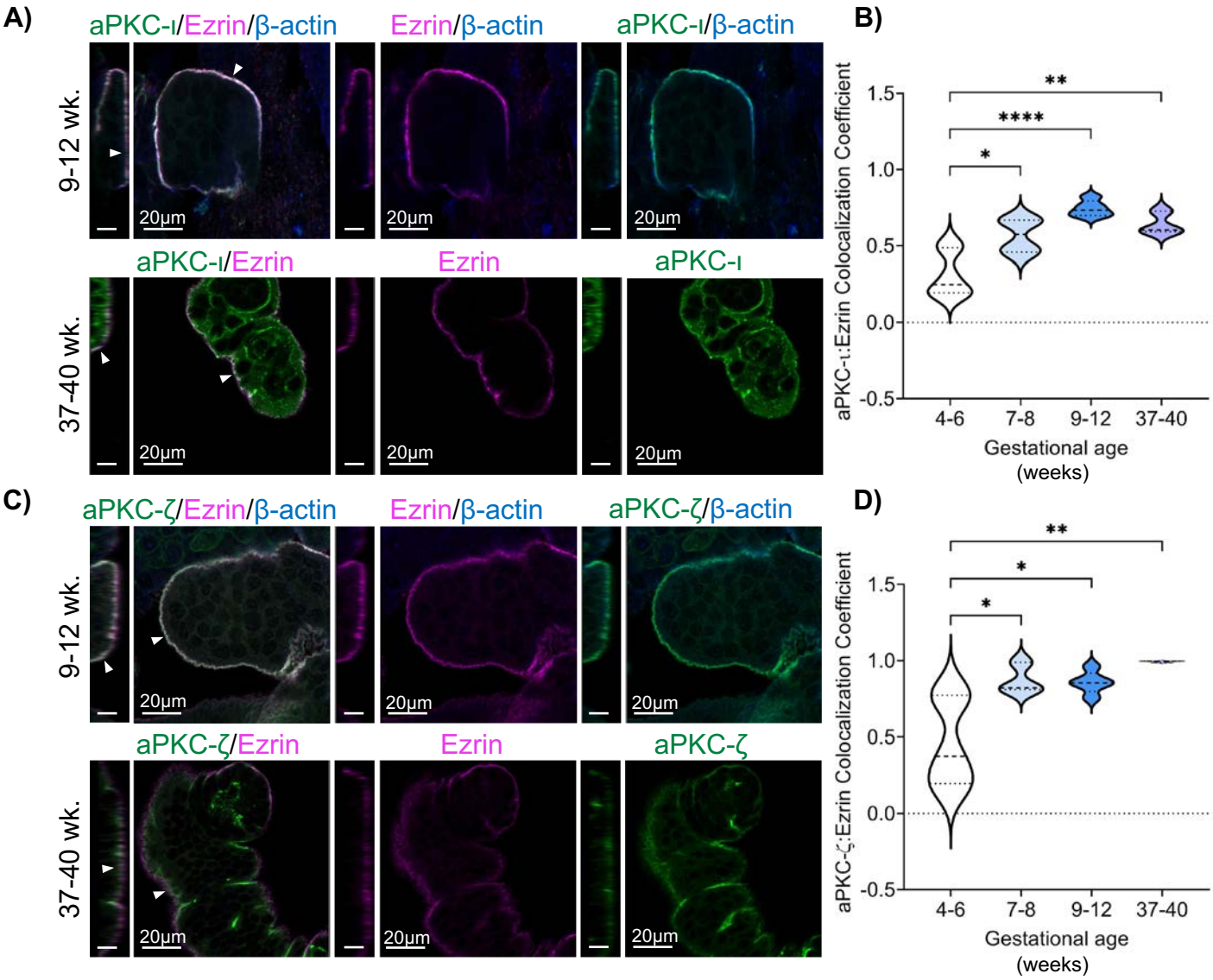
A)
aPKC-ι/Ezrin/β-actin
Ezrin/β-actin
aPKC-ι/β-actin
9-12 wk.
20μm
aPKC-ι/Ezrin
Ezrin
aPKC-ι
37-40 wk.
B)
aPKC-ι:Ezrin Colocalization Coefficient
1.5
1.0
0.5
0.0
-0.5
**
****
*
4-6
7-8
9-12
37-40
Gestational age
(weeks)
C)
aPKC-ζ/Ezrin/β-actin
Ezrin/β-actin
aPKC-ζ/β-actin
aPKC-ζ/Ezrin
Ezrin
aPKC-ζ
D)
aPKC-ζ:Ezrin Colocalization Coefficient

Figure 2:

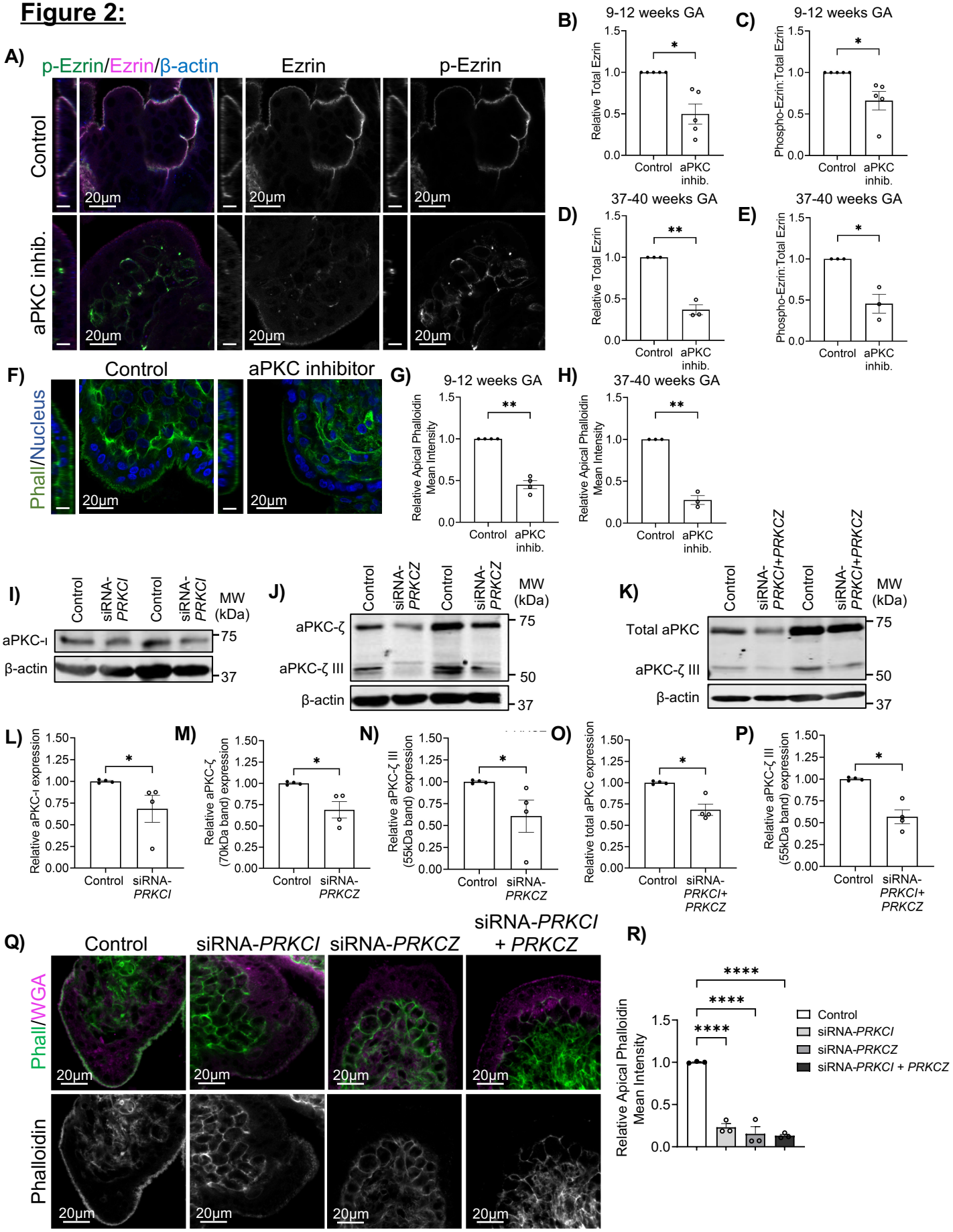
A)
p-Ezrin/Ezrin/β-actin
Ezrin
p-Ezrin
Control
aPKC inhib.
20µm
B)
9-12 weeks GA
Relative Total Ezrin
Control
aPKC inhib.
C)
9-12 weeks GA
Phospho-Ezrin:Total Ezrin
D)
37-40 weeks GA
E)
37-40 weeks GA
F)
Control
aPKC inhibitor
Phall/Nucleus
G)
9-12 weeks GA
Relative Apical Phalloidin Mean Intensity
H)
37-40 weeks GA
I)
Control
siRNA-PRKCI
MW (kDa)
aPKC-ι
β-actin
75
37
J)
siRNA-PRKCZ
aPKC-ζ
aPKC-ζ III
50
K)
siRNA-PRKCI+PRKCZ
Total aPKC
L)
Relative aPKC-ι expression
M)
Relative aPKC-ζ (70kDa band) expression
N)
Relative aPKC-ζ III (55kDa band) expression
O)
Relative total aPKC expression
P)
Q)
siRNA-PRKCI + PRKCZ
Phall/WGA
Phalloidin
R)
Control
siRNA-PRKCI
siRNA-PRKCZ
siRNA-PRKCI + PRKCZ

Figure 3:

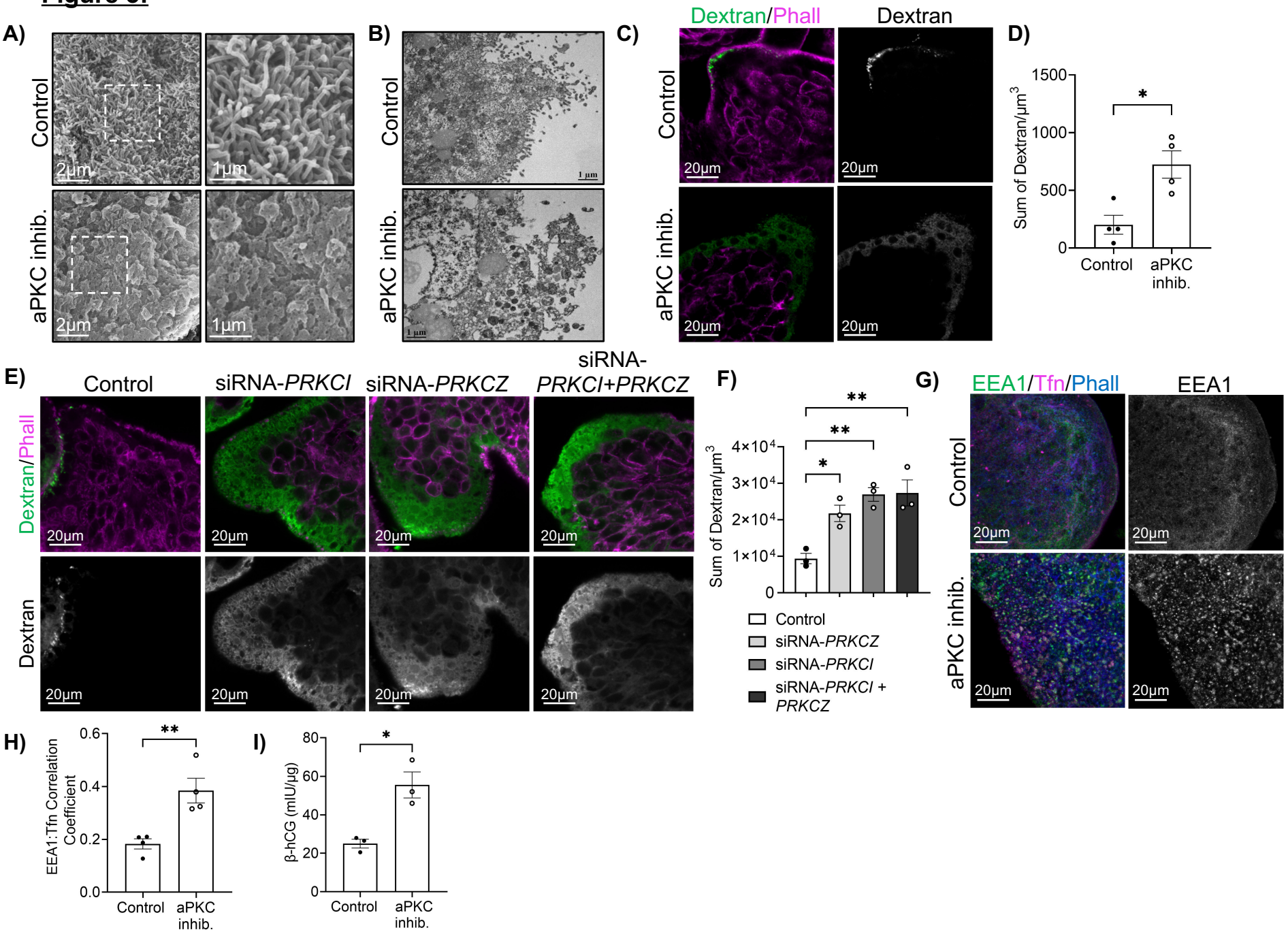
A)
Control
aPKC inhib.
2µm
1µm
B)
Control
aPKC inhib.
1 µm
C)
Dextran/Phall
Dextran
Control
aPKC inhib.
20µm
D)
Sum of Dextran/µm3
1500
1000
500
0
*
Control
aPKC inhib.
E)
Control
siRNA-PRKCI
siRNA-PRKCZ
siRNA-PRKCI+PRKCZ
Dextran/Phall
Dextran
20µm
F)
Sum of Dextran/µm3
4×10^4
3×10^4
2×10^4
1×10^4
0
*
**
**
Control
siRNA-PRKCZ
siRNA-PRKCI
siRNA-PRKCI + PRKCZ
G)
EEA1/Tfn/Phall
EEA1
Control
aPKC inhib.
20µm
H)
EEA1:Tfn Correlation Coefficient
0.6
0.4
0.2
0.0
**
Control
aPKC inhib.
I)
β-hCG (mIU/µg)
80
60
40
20
0
*
Control
aPKC inhib.

Figure 4:

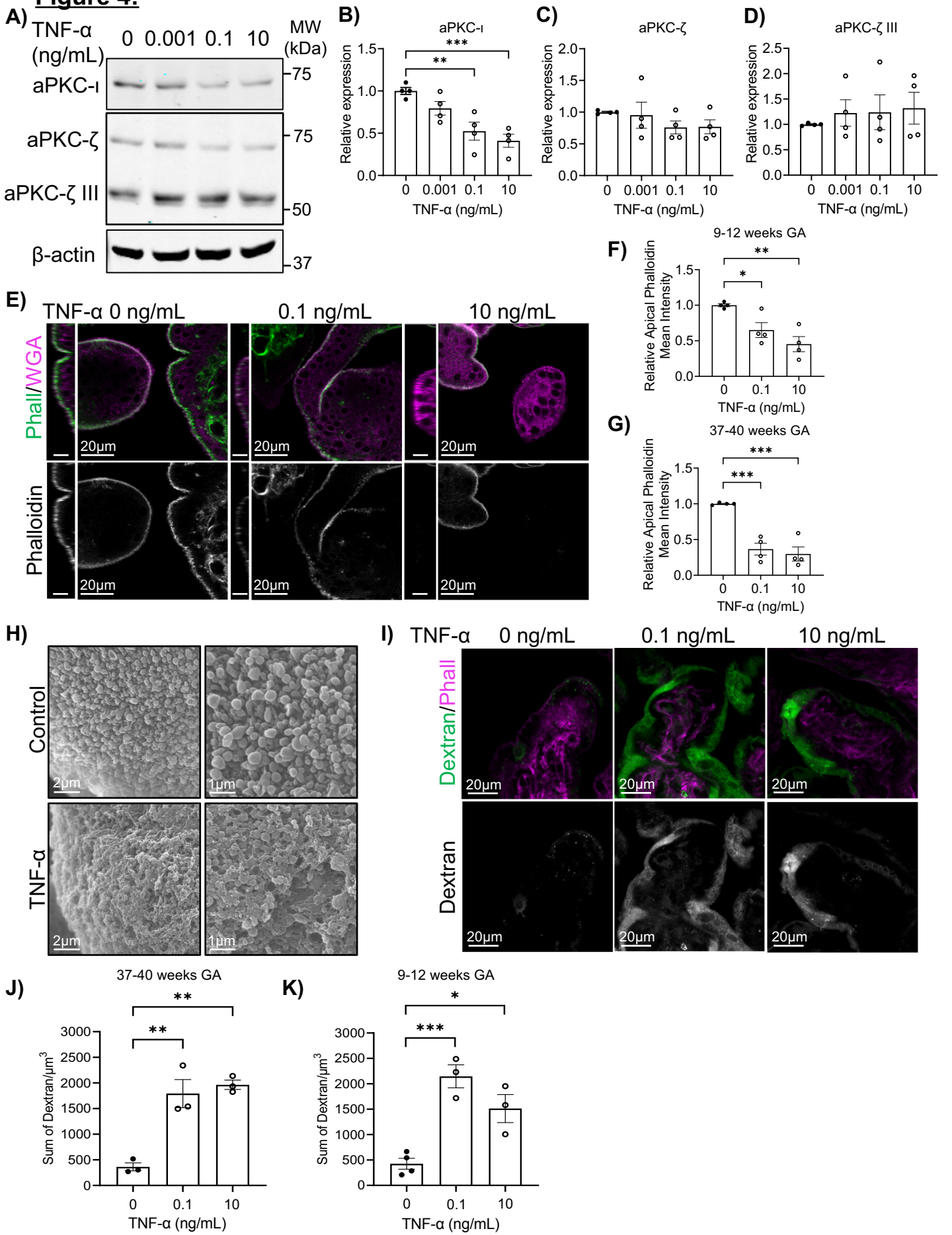
A)
TNF-α (ng/mL)
0 0.001 0.1 10
MW (kDa)
aPKC-ι
aPKC-ζ
aPKC-ζ III
β-actin
75
75
50
37
B)
aPKC-ι
Relative expression
TNF-α (ng/mL)
C)
aPKC-ζ
D)
aPKC-ζ III
E)
TNF-α 0 ng/mL
0.1 ng/mL
10 ng/mL
Phall/WGA
Phalloidin
20μm
F)
9-12 weeks GA
Relative Apical Phalloidin Mean Intensity
G)
37-40 weeks GA
H)
Control
TNF-α
2μm
1μm
I)
TNF-α 0 ng/mL
0.1 ng/mL
10 ng/mL
Dextran/Phall
Dextran
20μm
J)
37-40 weeks GA
Sum of Dextran/μm3
K)
9-12 weeks GA

Figure 5:

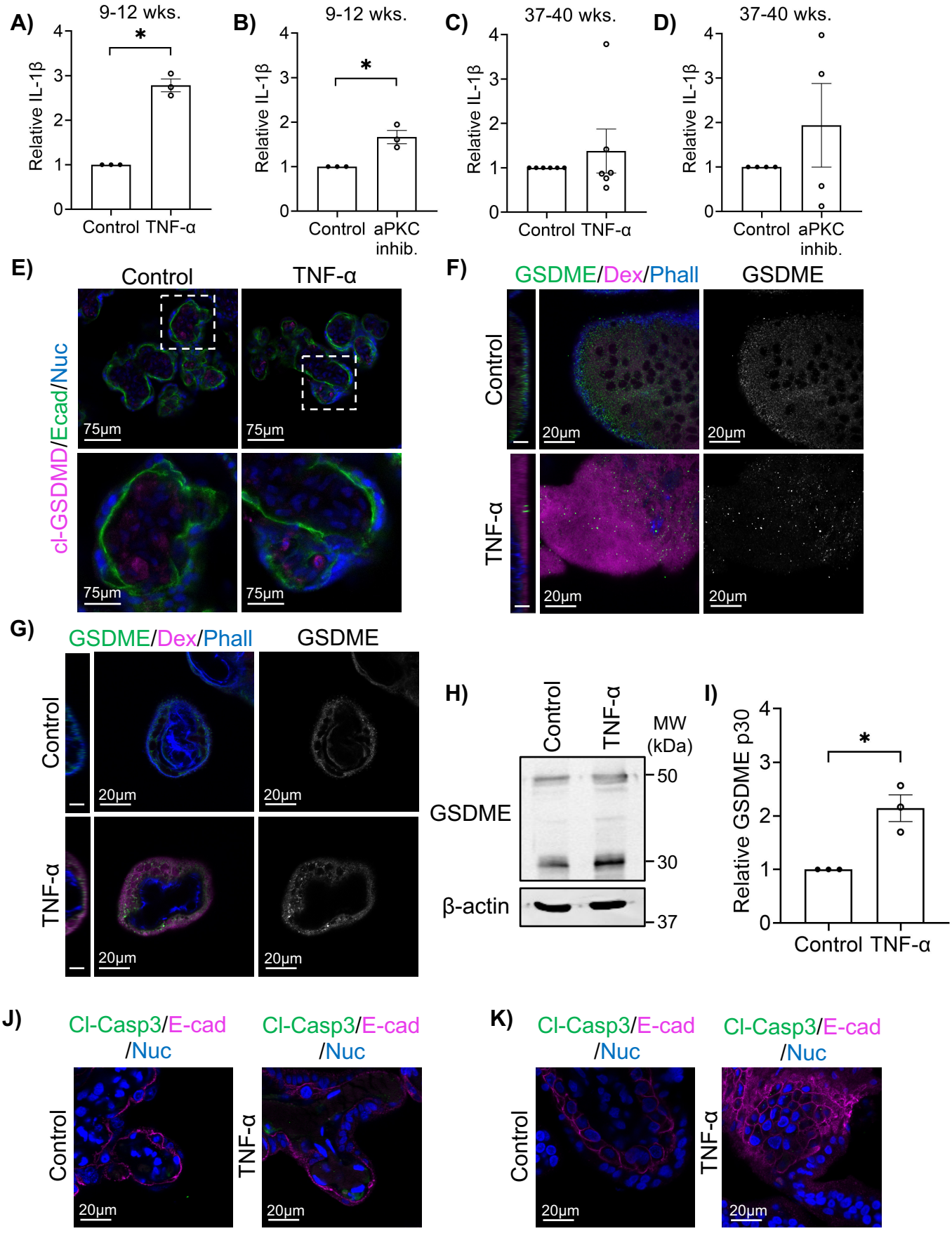
A)
9-12 wks.
Relative IL-1β
Control
TNF-α
B)
9-12 wks.
aPKC inhib.
C)
37-40 wks.
D)
37-40 wks.
E)
Control
TNF-α
cl-GSDMD/Ecad/Nuc
75μm
F)
GSDME/Dex/Phall
GSDME
20μm
G)
H)
MW (kDa)
GSDME
β-actin
50
30
37
I)
Relative GSDME p30
J)
Cl-Casp3/E-cad /Nuc
K)

Figure 6:

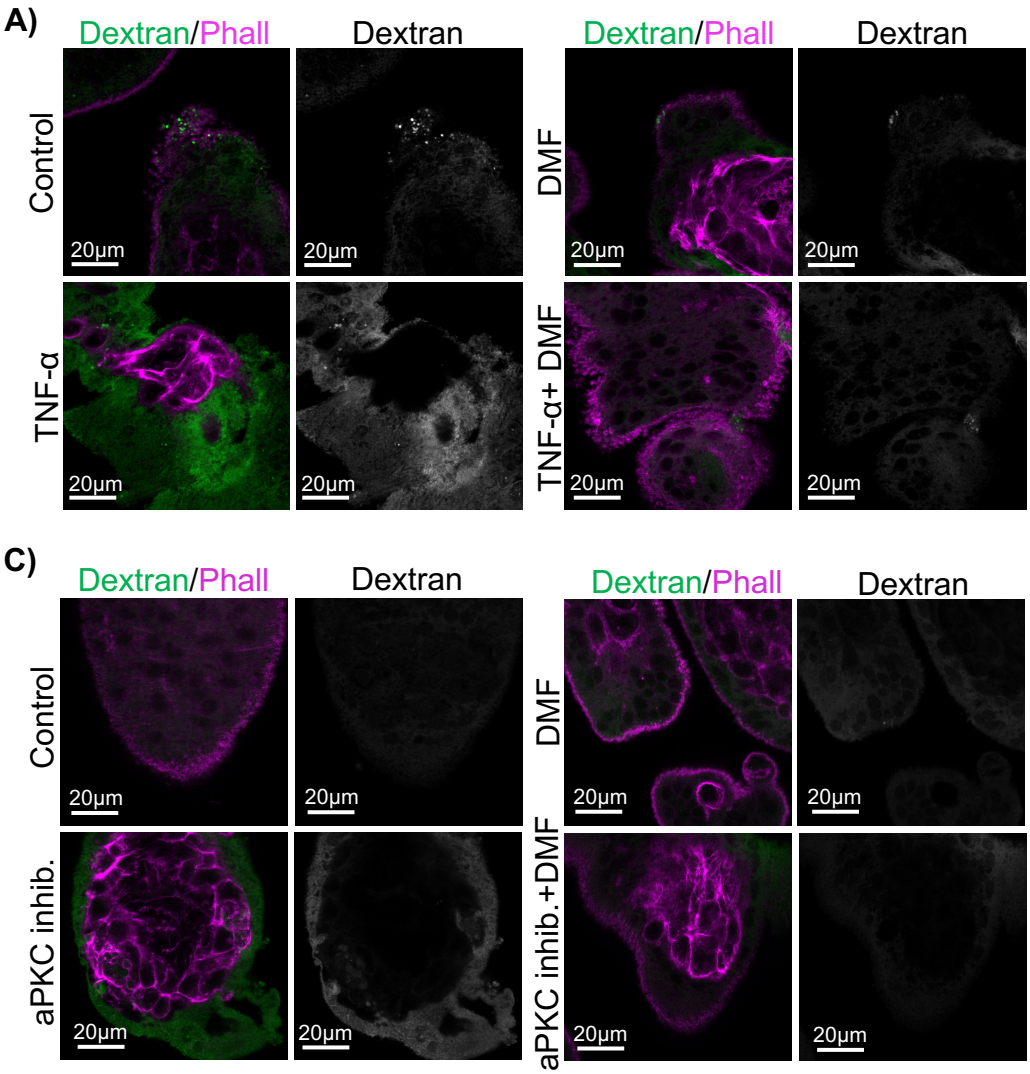
A)
Dextran/Phall
Dextran
Control
DMF
TNF-α
TNF-α+ DMF
20µm
C)
aPKC inhib.
aPKC inhib.+DMF

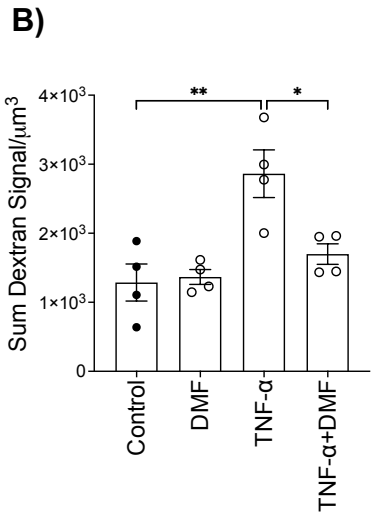
B)
Sum Dextran Signal/µm3
4×10³
3×10³
2×10³
1×10³
0
**
*
Control
DMF
TNF-α
TNF-α+DMF

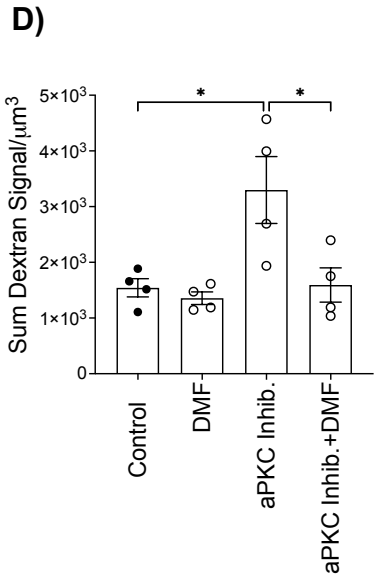
D)
Sum Dextran Signal/µm3
5×10³
4×10³
3×10³
2×10³
1×10³
0
*
*
Control
DMF
aPKC Inhib.
aPKC Inhib.+DMF